rather little on the degree of grafting, especially if the latter is low. For this reason, it cannot be decided unambiguously if the grafting model discussed here is completely adequate to physical reality. No papers concerned with a detailed experimental study of molecular parameters of graft copolymers could be found in the literature. It is believed, therefore, that any contribution dealing with the subject may appear useful.

Registry No. (Methyl methacrylate)·(styrene) (copolymer), 25034-86-0.

References and Notes

(1) Vorliček, J.; Kratochvil, P. *J. Polym. Sci., Polym. Phys. Ed.* **1973**, *11*, 1251.
(2) Tung, L. H.; Wiley, R. M. *J. Polym. Sci., Polym. Phys. Ed.* **1973**, *11*, 1413.
(3) Ikada, Y.; Horii, F. *Makromol. Chem.* **1974**, *175*, 227.
(4) (a) Shultz, A. R. Report No. 78CRD003, General Electric Co., Schenectady, NY, 1978. (b) Shultz, A. R. *Polym. Prepr., Am. Chem. Soc., Div. Polym. Chem.* **1979**, *20* (2), 179. (c) Shultz, A. R. Contribution presented at the 24th Prague Microsymposium on Macromolecules; Prague, 1983; Abstract No. 24.
(5) Kotaka, T.; Donkai, N.; Min, T. I. *Bull. Inst. Chem. Res. Kyoto Univ.* **1974**, *52*, 332.
(6) Orofino, T. A. *Polymer* **1961**, *2*, 295.
(7) Zimm, B. H.; Stockmayer, W. H. *J. Chem. Phys.* **1949**, *17*, 1301.
(8) Inagaki, H.; Tanaka, T. In "Developments in Polymer Characterization-3"; Dawkins, J. V., Ed.; Applied Science Publishers: Barking, 1982.
(9) Stejskal, J.; Kratochvil, P. *Polym. J.* **1982**, *14*, 603.
(10) Tuzar, Z.; Kratochvil, P. *Adv. Colloid Interface Sci.* **1976**, *6*, 201.
(11) Jones, M. H. *Can. J. Chem.* **1956**, *34*, 948.
(12) Ohnuma, H.; Kotaka, T.; Inagaki, H. *Polymer* **1969**, *10*, 501.
(13) Kratochvil, P.; Sedláček, B.; Straková, D. *Makromol. Chem.* **1971**, *148*, 271.

Characterization of Poly(methyl methacrylate) during the Thermal Polymerization of Methyl Methacrylate

Ben Chu* and Day-chyuan Lee

Chemistry Department, State University of New York at Stony Brook, Long Island, New York 11794.

Received August 11, 1983

ABSTRACT: During the thermal polymerization of MMA, we have been able to investigate both the static and the dynamic properties of the polymer formed, poly(methyl methacrylate) (PMMA), in terms of the molecular weight M_w, the second virial coefficient A_2, the radius of gyration R_g, the translational diffusion coefficient D_T and its corresponding equivalent hydrodynamic radius R_h, and estimates of the size (or molecular weight) distribution of PMMA in dilute solution and in terms of the isothermal compressibility $(\partial\pi/\partial C)_{P,T}$, the cooperative diffusion coefficient D_c, and a slow characteristic decay time which mimics but is not the self-diffusion coefficient D_s in the semidilute solution regime. By combining a spectroscopic technique such as Raman scattering, which can determine the polymer concentration noninvasively during the polymerization process, with laser light scattering, we have demonstrated a viable procedure for on-line monitoring of solution polymerization processes, permitting us to investigate detailed macromolecular properties in solution polymerization kinetics.

I. Introduction

Studies of polymerization processes have been difficult because we lack a convenient probe which we can use one-line to monitor the concentrations of the monomer(s) and of the polymer in a polymerization reaction. Spectroscopic techniques such as NMR, IR, Raman, and fluorescence and other physical methods such as density and surface tension offer reasonable and possible alternatives which permit us to measure the appropriate concentration of species in a chemical reaction. However, in a polymerization process, we really want to know not only the concentrations of the monomer (C_m) and of the polymer (C_p) but also molecular parameters such as the molecular weight M of the polymer product during the chemical reaction.

The aim of this article is directed at an important need in chemical reactor engineering; i.e., we try to link together an application of several established results in Raman scattering and laser light scattering and hopefully to demonstrate that development of an on-line technique for characterizing the polymer product during the course of the polymerization reaction is a worthwile undertaking even though it is likely to be a difficult one from practical viewpoints. Nevertheless, as informative on-line measurements of important molecular parameters of the polymer product often represent the major stumbling block to control of polymerization processes, an establishment of measurements on accessible molecular parameters of the polymer product in our proposed scheme under even ideal conditions becomes of interest.

It should be recognized that our measurement scheme is limited mainly to solution and bulk polymerization processes and that we have neglected convective motions which often exist in a chemical reactor. Such convective motions, which could be produced by flow of reactant(s) and product(s) and/or by thermal gradients, would invariably affect the light scattering spectrum and the translational diffusive motions of the polymer product(s). However, these problems may be resolved by varying experimental conditions or they can be investigated for specific systems. For example, flow can be measured by using laser Doppler velocimetry[1] and thermal gradients can be alleviated by changing the chemical reaction vessel design.

In this paper, we report some of the results of our studies on the thermal polymerization of methyl methacrylate (MMA) using a combination of Raman scattering and laser light scattering[1] whereby we have been able to measure many of the main variables of interest in terms of known molecular parameters, namely, the rate of conversion, the weight-average molecular weight M_w of the polymer product, poly(methyl methacrylate) (PMMA), and esti-

0024-9297/84/2217-0926$01.50/0

mates of the polymer polydispersity. Furthermore, due to the specific nature of the polymerization process, i.e., for free radical polymerization, we know the molecular weight of the polymer formed to remain relatively constant, we have been able to establish Zimm plots in dilute solutions and to determine both the second virial coefficient A_2 and the radius of gyration R_g in addition to the weight-average molecular weight. In the same dilute solutions, precise measurements of the time correlation function permit us to determine the z-average translational diffusion coefficient $\bar{D}_T$, its corresponding equivalent hydrodynamic radius $\bar{R}_h$, and the polydispersity index $(\mu_2/\bar{\Gamma}^2)$ as well as to estimate the line width distribution function $G(\Gamma)$, which is related to the hydrodynamic size (or the molecular weight) distribution. At higher solution concentrations in the semidilute regime, we have succeeded in determining the osmotic compressibility $(\partial\pi/\partial C)_{P,T}$ and the cooperative diffusion coefficient D_c and in confirming the existence of a very slow characteristic decay time which mimics but is not the self-diffusion coefficient D_s as a function of concentration (time). As the very slow characteristic decay time has a size dependence, more careful time correlation function profile analysis also suggests a scheme whereby we can estimate size polydispersity from a correlation function profile analysis of the slow mode in semidilute solutions. It should be emphasized that we have not yet completed our development of a practical *concentration* and *molecular parameter* probe for polymerization process control. The present article is concerned mainly with the potential of such a scheme under relatively ideal conditions.

II. Theoretical Rationale

Light scattering and Raman spectroscopic techniques have been used to study the thermal polymerization of styrene.[2,3] The techniques are noninvasive and can share the same light source and detection electronics.

1. Raman Spectroscopy. Raman spectroscopy has been a useful tool to elucidate the structure of polymers. On occasion, it has been used to determine concentrations of monomer sequences in copolymers.[4] In a chemical reaction, some bonds are broken and others are being formed while most remain relatively unchanged. Therefore, Raman peaks which are characteristic of the respective chemicals of interest can be used to monitor the concentrations of those chemicals, while the peaks which show no change during the polymerization process can be used to monitor the laser incident intensity and act as some form of an internal built-in reference standard useful for normalization purposes. On closer examination, Raman polymer peaks may depend on other factors in addition to polymer concentration, and the location and shape of Raman peaks may change slightly due to structural variations during the polymerization process. Therefore, in using the Raman spectroscopic technique as a probe to monitor concentration of chemical species, we should also use other analytical analysis to confirm the scheme.

2. Intensity of Scattered Light.[5] The Rayleigh ratio (R_{vu}) for vertically polarized incident and unpolarized scattered light at finite concentrations in dilute solution has the approximation form

$$\frac{HC}{R_{vu}} = (M_w^{-1} + 2A_2C)\left(1 + \frac{16\pi^2n^2}{3\lambda_0^2}R_g^2 \sin^2\left(\frac{\theta}{2}\right)\right) \quad (1)$$

where H, in units of mol cm^2 g^{-2}, is equal to $4\pi^2n^2(\partial n/\partial C)^2/(N_A\lambda_0^4)$, with n, C (g/cm^3), N_A, λ_0, and $\partial n/\partial C$ being the respective refractive index, concentration, Avogadro's number, wavelength in vacuo, and refractive index increment; R_{vu} (cm^{-1}) is the excess Rayleigh ratio due to concentration fluctuations of the polymer solution using vertically polarized incident and unpolarized scattered light; M_w is the weight-average molecular weight, A_2 (mol cm^3 g^{-2}) is the second virial coefficient, and R_g (cm) is the root-mean-square radius of gyration.

According to eq 1, the second virial coefficient A_2, the weight-average molecular weight M_w, and the radius of gyration R_g can be determined by using a Zimm plot whereby

$$\lim_{C\to 0}\frac{HC}{R_{vu}} = \frac{1}{M_w}\left(1 + \frac{K^2R_g^2}{3}\right) \quad (2)$$

$$\lim_{\theta\to 0}\frac{HC}{R_{vu}} = \frac{1}{M_w} + 2A_2C \quad (3)$$

and

$$\lim_{\substack{C\to 0\\ \theta\to 0}}\frac{HC}{R_{vu}} = \frac{1}{M_w} \quad (4)$$

where K $[=(4\pi/\lambda)\sin(\theta/2)$, with $\lambda = \lambda_0/n]$ is the magnitude of the momentum transfer vector. Equation 1 is no longer valid at higher concentrations. However, we can write

$$\lim_{K\to 0}\frac{HC}{R_{vu}} = \frac{1}{RT}\left(\frac{\partial\pi}{\partial C}\right)_{T,P} \quad (5)$$

where the concentration-dependent osmotic compressibility term, $(\partial\pi/\partial C)_{T,P}$, is independent of the polymer molecular weight, at least for specific polymer solutions in a good solvent.

3. Spectrum of Scattered Light.[5,6] The light scattering spectrum of a polymer solution contains a wealth of information which can be related to the translational, and possibly rotational, motion as well as many forms of internal motions of the polymer molecules. We shall limit our discussion to photon correlation measurements.

The measured single-clipped photoelectron count autocorrelation function for a detector of finite effective photocathode has the form

$$G_k^{(2)}(\tau) = N_s\langle n_k\rangle\langle n\rangle(1 + b|g^{(1)}(\tau)|^2) \quad (6)$$

where $g^{(1)}(\tau)$ is the first-order normalized time correlation function of the scattered electric field, k is the clipping level, τ is the delay time, $\langle n_k\rangle$ and $\langle n\rangle$ are mean clipped and unclipped counts per sample time, and N_s is the total number of samples with the base line $A = N_s\langle n_k\rangle\langle n\rangle$. $N_s\langle n_k\rangle$ and $N_s\langle n\rangle$ are the total clipped counts and total unclipped counts, respectively. b is a spatial coherence factor, depending upon various experimental conditions such as coherence and receiver areas, and is usually taken as an unknown parameter in the data-fitting procedure. Equation 6 is valid for an extensive class of signals having Gaussian field probability distribution.[6]

For a monodisperse sample of noninteracting macromolecules in solution (or colloidal particles in suspension)

$$(Ab)^{1/2}g^{(1)}(K,\tau) \propto I(K)\exp(-\Gamma(K)\tau) \quad (7)$$

where the scattered intensity $I(K) = Ni(K)$, with N and i being the number of macromolecules in the scattering volume V and the scattered intensity from each macromolecule, respectively. Γ $(=D_TK^2$ when $KR_g \ll 1)$ is the characteristic line width, with D_T (cm^2 s^{-1}) being the translational diffusion coefficient. At finite but dilute concentrations and in the presence of interactions

$$D = D_0(1 + k_dC) \quad (8)$$

where D_0 is the diffusion coefficient at infinite dilution. The hydrodynamic and thermodynamic factors are combined in the second virial coefficient for diffusion k_d, which is system specific. The subscript T has been dropped.

In semidilute solution and in the small KR_g range, which avoids the complication of internal polymer motions, the time correlation functions measures the cooperative diffusion coefficient D_c and another much slower relaxation time which has been related to the self-diffusion coefficient D_s.[7-9] Identity of this slow relaxation time to D_s has been open for discussion. We shall refer to a brief listing of current results in the Conclusion. Suffice it to say that the measured slow relaxation time can be utilized to characterize molecular (or clustering) properties of the polymer product formed in semidilute solutions regardless of the source of discrepancy. Generally, we can express D_c and D_s to be in their respective pseudogel ($K\xi_c \ll 1$) and reptation ($KR_g \ll 1$) regimes, with ξ_c being the screening length of concentration blobs. The cooperative diffusion coefficient is independent of molecular weight and is proportional to $C^{3/4}$ and C^1 in semidilute-good and semidilute-Θ solvents, respectively. On the other hand, the self-diffusion coefficient depends on the molecular weight and we have, according to the scaling concept

$$\begin{aligned} D_s &= k_s M^{-2} C^{-7/4} && \text{semidilute-good region} \\ &= k_s^* M^{-2} C^{-3} && \text{semidilute-}\Theta\text{ region} \end{aligned} \tag{9}$$

where k_s and k_s^* are proportionality constants. Therefore, under appropriate conditions, perhaps eq 9 can suggest a scheme to calibrate the molecular weight and its polydispersity of the polymer product at semidilute concentrations.

4. Correlation Function Profile Analysis.[10-12] For a polydisperse sample

$$|g^{(1)}(\tau)| = \int_0^\infty G(\Gamma) \exp(-\Gamma\tau)\, d\Gamma \tag{10}$$

where $G(\Gamma)$ is the normalized distribution of decay rates. In practice, eq 10 uses a measured $|g^{(1)}(\tau)|$ which has noise and is bandwidth limited. Furthermore, the limits of integration have both upper and lower bounds, yielding

$$|g^{(1)}(\tau)| = \int_a^b G(\Gamma) \exp(-\Gamma\tau)\, d\Gamma \tag{10'}$$

As the Laplace transform of eq 10′ is ill-conditioned, we can only approximate $G(\Gamma)$ using methods which can put further constraints on the problem. In this article, we shall consider only the multiexponential approach with solutions to be evaluated by the singular-value decomposition method.[11] We approximate $G(\Gamma)$ as a sum of equally spaced single exponentials

$$G(\Gamma) \propto \sum_{j=1}^{m} I_j \delta(\Gamma - \Gamma_j) \tag{11}$$

or as a sum of logarithmically spaced single exponentials

$$G(\Gamma) \propto \sum_{j=1}^{m} I_j^* \delta(\ln \Gamma - \ln \Gamma_j) \tag{12}$$

where m is a small number, usually 3 or 4, depending upon the signal-to-noise ratio of $g^{(1)}(\tau)$ and the b/a ratio. The superscript asterisk signifies a change of variable from Γ to ln Γ. According to eq 4 and $I(K) = Ni(K)$, we have

$$N_j(M_j) \propto I_j(M_j)/M_j^2 \tag{13}$$

where $N_j(M_j)$ is the number of representative polymer molecules with molecular weight M_j and $I_j(M_j)$ is the corresponding scattered intensity from N_j polymer molecules. In eq 13, we have taken the limit of $K \to 0$ and $C \to 0$. In dilute solution, first-order correction due to the contributions from $P(KR_g)$ and A_2 can be introduced. Then, we have

$$N_j(M_j) \propto I_j(M_j)[1 + K^2 R_{g,j}^2(M_j)/3 + 2\bar{A}_2 C M_j]/M_j^2 \tag{14}$$

where we have taken $P^{-1} \approx 1 + K^2 R_g^2/3$ and $\bar{A}_2$ to be the measured second virial coefficient over the concentration range of eq 1.

Having obtained an estimate of the normalized distribution of translational diffusion coefficient $G(D)$, we define the number molecular weight distribution

$$F_n(M_j) = \sum_{j=1}^{m} N_j \delta(M - M_j) \tag{15}$$

and relate each representative translational diffusion coefficient, D_j, with a molecular weight, M_j, and a characteristic molecular parameter, X_j ($\equiv KR_{g,j}$), by use of the following molecular weight scaling laws[13] for D and R_g:

$$D = k_D M^{-\alpha_D} \tag{16}$$

$$R_g = k_R M^{\alpha_R} \tag{17}$$

The two scaling laws are also closely tied to the intrinsic viscosity scaling law exponent such that if $[\eta] = k_\eta M^{\alpha_\eta}$, $\alpha_D = (1 + \alpha_\eta)/3$. We can evaluate the preexponential factors k_D and k_R by using the measured values of M_w and R_g from static light scattering studies provided that α_D and α_R are known. In the iterative procedure, we first estimated k_D by assuming that $P(X) = 1$ and then adjusted k_R by comparing the measured and computed R_g values using the first approximate $F_n(M_j)$. We then vary k_D by comparing the measured and computed values of M_w. The iterative procedure was terminated when a k_D value could yield an $M_{w,cald}$ which was in agreement with the measured M_w from our static light scattering measurements. For completeness we note that

$$M_{w,cald} = \sum N_j M_j^2 / \sum N_j M_j \tag{18}$$

$$R_{g,cald} = k_R \sum N_j M_j^{(2+\alpha_R)} / \sum N_j M_j^2 \tag{19}$$

and

$$F_{w,cum}(M) = \int_M^\infty F_n(M) M\, dM / \int_0^\infty F_n(M) M\, dM \tag{20}$$

where $F_{w,cum}(M)$ is the normalized cumulative weight-average molecular weight distribution.

In the semidilute solution regime, eq 9 suggests a possibility to estimate information on the polymer molecular weight and perhaps even its polydispersity. Since we can determine the concentration using Raman spectroscopy, we should be able to calibrate k_s from one simultaneous analysis of D_s and M for a specific polymer solution at temperature T. Once k_s is known for the system, it becomes feasible to estimate M from measurements of the self-diffusion coefficient D_s and C from Raman spectroscopy. There is an experimental limitation in the concentration range to which this approach is practical because the characteristic time related to D_s is very slow in semidilute solutions.

An approximate estimate to the polydispersity effect from D_s may be explored as follows. At some overall concentration, we may write

$$\langle D_s \rangle = k_s \sum N_j M_j^2 M_j^{-2} / \sum N_j M_j^2 \tag{21}$$

where we have assumed $I_{j,s} \propto N_j M_j^2$ to remain valid in

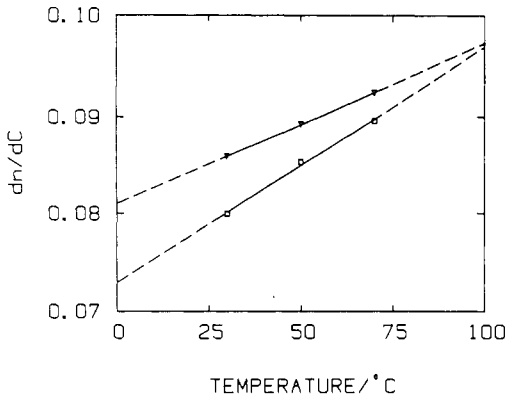

Figure 1. Plot of dn/dC vs. temperature for PMMA in MMA at λ_0 = 436 nm (▽) and λ_0 = 546 nm (□).

semidilute solutions since the molecular weight dependence of $I_{j,s}$ due to self-diffusion only is not known. Nevertheless, eq 21 can be simplified in terms of M_w and M_n to

$$\langle D_s \rangle = k_s^*/(M_n M_w) \tag{21'}$$

Similarly

$$\langle D_s^2 \rangle = k_s^{*2}(M_{-w}M_{-n})^{-1}(M_n M_w)^{-1} \tag{22}$$

where

$$M_{-w}^{-1} = \sum N_j M_j^{-2}/\sum N_j M_j^{-1} \tag{23}$$

$$M_{-n}^{-1} = \sum N_j M_j^{-1}/\sum N_j \tag{24}$$

Thus, we have for the variance $\mu_2/\bar{\Gamma}^2$ in D_s

$$\frac{\langle D_s^2 \rangle}{\langle D_s \rangle^2} - 1 = \frac{M_w M_n}{M_{-w}M_{-n}} - 1 \tag{25}$$

a curious index, which nonetheless depends upon the polydispersity.

III. Experimental Methods

Raman spectra were obtained with a conventional Spex 1302 double-monochromator (0.5 m, 1200 grooves/mm). The Raman spectrometer was modified to accept a high-temperature cell for the thermal polymerization of MMA and to measure the absolute light scattering intensity and spectrum at four different scattering angles. The details will be described in a subsequent article on polyphosphazene reactions where the temperature can be controlled to ±0.5 at 250 °C. Both Raman scattering and light scattering intensity measurements were recorded and controlled by a HP 9830 calculator. We used an argon ion laser operating at 448.0 nm as the incident light source for both Raman and light scattering measurements. Integrated scattered intensities were measured by a standard photon-counting detection system while the single-clipped photoelectron count autocorrelation function was measured with a Malvern K7023 correlator. Temperatures were controlled to ±0.01 °C near room temperature and to ±0.05 °C at high temperatures.

Among the three samples we have studied, sample 2 was degassed by several freeze–pump cycles, with the inhibitor (hydroquinone monomethyl ether) being left undisturbed. Both sample 1 and sample 3 were first distilled, adding 1 drop of mother undistilled MMA in order to introduce a trace amount of the inhibitor and then degassed. The trace amount of inhibitor provided time for us to manipulate the MMA before the polymerization reaction could start. All solutions were filtered through a Millipore filter of nominal 0.22-μm pore diameter before measurements.

We used benzene as a reference for computing the Rayleigh ratio R_{vu} and took $R_{vu} = R_{vv} + R_{vh} = 3.86 \times 10^{-5}$ cm^{-1} [14] for benzene at θ = 90°, λ_0 = 488 nm, and 23 °C.

The refractive index of MMA at λ_0 = 488 nm was estimated to be 1.3731 and 1.3999 at 90 and 50 °C, respectively. $\partial n/\partial C$ was determined with a Brice Phoenix differential refractometer at two different wavelengths (436 and 546 nm) and three different temperature (30, 50, and 70 °C) as shown in Figure 1. By extrapolation, we estimated $\partial n/\partial C$ = 0.100 at 90 °C and $\partial n/\partial C$ = 0.0838 at 50 °C. The densities of MMA and of PMMA were adopted from the "Polymer Handbook", which showed values of 0.880 and 0.918 g/cm^3 for MMA and values of 1.171 and 1.182 g/cm^3 for PMMA at 90 and 50 °C, respectively. The viscosities of MMA are 0.26 and 0.42 cP at 90 and 50 °C, respectively.

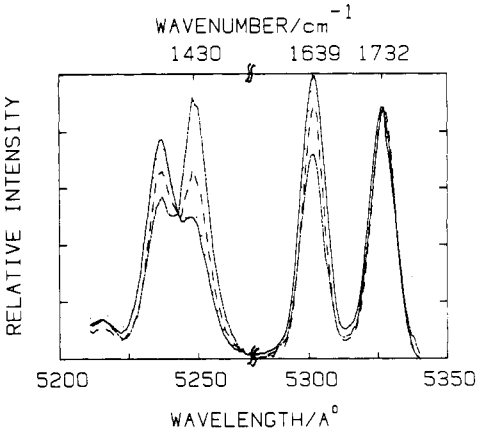

Figure 2. Several Raman spectra obtained during the course of thermal polymerization of MMA at 50 °C showing the decrease in C=C peak at 1639 cm^{-1} and the constant intensity in the C=O peak at 1732 cm^{-1} for sample 3 at 13 h (solid line), 54.5 h (dotted line), 266 h (dashed line), and 351 h (dash–dot line). A more complex polymer peak at 1430 cm^{-1} is not being evaluated in this study, partly because the polymer peak may depend on macromolecular properties, partly because we have been interested in conversion studies up to <50% completion before the laser incident intensity damages the polymer glass being formed, and partly because the peak overlaps with another monomer peak.

IV. Results and Discussion

Raman spectra were used to determine the concentration of the reactant (monomer) and of the product (polymer). From the product formed as a function of time, we can study the kinetics of polymerization processes in terms of conversion and the Trommsdorf effect. In dilute solutions, we can make full use of light scattering intensity and line width data to obtain many of the pertinent molecular parameters of the polymer formed during the polymerization process. At higher concentration ($C > C^*$) where polymer coils overlap, we have made use of D_s to infer the molecular weight of the polymer product in semidilute solutions.

1. Raman Spectra. We first measured the Raman spectra of the monomer MMA and of the polymer PMMA. We then selected the 1732-cm^{-1} peak due to the carbon–oxygen double bond (C=O) stretching as our internal standard and the aliphatic carbon–carbon double bond (C=C) at 1639 cm^{-1} as a probe for the monomer concentration. Figure 2 shows several Raman spectra obtained during the thermal polymerization of MMA at 50 °C. The decrease in the C=C peak at 1639 cm^{-1} with increasing time shows that the monomers are being used up during the polymerization process while the relatively constant peak of the C=O bond at 1732 cm^{-1} confirms that our entire light scattering system has remained stable over extended periods of time, i.e., over a period of 15 days. Laser intensity stability is not an important issue here because we can always use the internal reference, C=O peak, to normalize the intensities of other peaks of interest. It was not necessary to have the laser on during the entire course of the experiment. The polymer peak at 1430 cm^{-1} reveals the formation of PMMA. However, in the initial stages, the appearance of a polymer peak has relatively low signal-to-noise advantages. So, a direct determination of

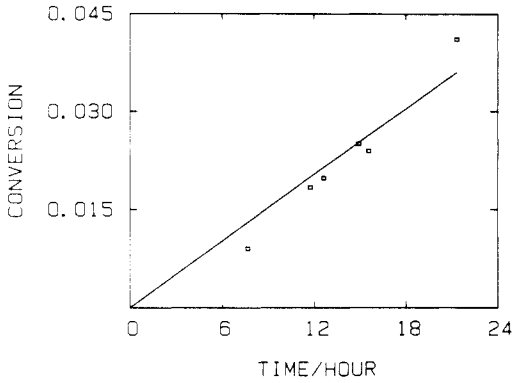

Figure 3. Fractional conversion of monomer vs. time obtained from the height change of the C=C peak for sample 1 reacted at 90 °C. The solid line is represented by eq 28 with a_1 listed in Table I.

the polymer concentration is more difficult to detect from the *appearance* of a Raman peak when the polymer concentration is low. Furthermore, it is not certain whether this polymer peak is independent of its molecular properties and depends only upon the polymer concentration. The overlapping neighboring monomer peak may also affect our evaluation of the polymer peak. It should be recognized that the polymer peak could yield useful information as the polymerization process progresses toward its complete conversion. However, we have not used the polymer peak in our present study.

In the Raman spectra, we have observed that the shape of the Raman peaks and the half-width of the monomer characteristic peak at 1639 cm^{-1} as well as that of the C=O bond stretching at 1732 cm^{-1} remains relatively unchanged. Although the fractional conversion of the monomer can best be determined by using the ratio of the integrated peak area of the C=C stretching intensity at 1639 cm^{-1} to that of the C=O reference peak at 1732 cm^{-1}, we have used the C=C peak height h_m and normalized it by the C=O peak height h_r in order to obtain the fractional conversion of the monomer f_m and the fractional conversion of the polymer f_p (=1 − f_m) with

$$f_m(t) = \frac{h_m(t)}{h_r(t)} \frac{h_r^0}{h_m^0} \tag{26}$$

where the superscript zero represents the peak height values at $t = 0$. The concentration of polymer formed, C_p (g/cm^3), has the form

$$C_p = f_p d_m d_p / (f_p d_m + f_m d_p) \tag{27}$$

where d_p and d_m are densities of PMMA and of MMA, in g/cm^3, respectively. In eq 27, we have assumed no interaction between PMMA and MMA; i.e., the volume of mixing is zero. Figure 3 shows a typical plot of initial fractional conversion of monomer as a function of time for sample 1 reacted at 90 °C. The approximate linear behavior is represented by

$$f_p = 1 - \exp(-a_1 t) \tag{28}$$

with the numerical values for a_1 listed in Table I. Samples 2 and 3 were reacted at 50 °C mainly for our own convenience because the lower reaction temperature permits us to have ample time to carry out our light scattering line width measurements and to check for reproducibility. Figure 4 shows plots of fractional conversion of monomer vs. time for samples 2 (with a large amount of inhibitor) and 3 (with only a trace amount of the inhibitor from 1 drop of undistilled MMA) at 50 °C. The induction period (much longer for sample 2) has been omitted in the plots.

Table I
Conditions and Fitting Parameters in Evaluating the Time Dependence of Fractional Conversion of Monomer during the Thermal Polymerization of MMA[a]

	sample[b]		
	1	2	3
temp, °C	90	50	50
a_1, h^{-1}	1.72×10^{-3}	4.85×10^{-4}	2.43×10^{-4}
a_2, g/cm^3		1.44×10^{-2}	6.25×10^{-3}
a_3, g/cm^3		6.89	2.67
a_4		−9.04	−8.45
a_5, h^{-1}		4.01×10^{-2}	1.83×10^{-2}

[a] Note: $f_p = 1 - \exp(-a_1 t)$ (eq 28) and $\ln [(f_p - a_2)/(a_3 - f_p)] = a_4 + a_5 t$ (eq 29). [b] Conditions (all samples were degassed): sample 1, distilled + 1 drop of undistilled MMA; sample 2, undistilled MMA (with inhibitor); sample 3, distilled + 1 drop of undistilled MMA.

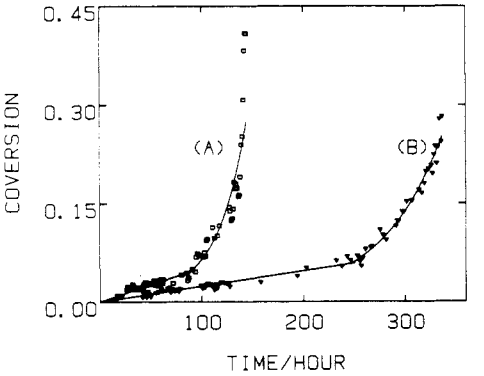

Figure 4. Fractional conversion of monomer vs. time obtained from the height change of C=C peak for sample 2 (□, experimental data; solid line A, fitted curve) and sample 3 (▽, experimental data; solid line B, fitted curve) at 50 °C. The solid lines A and B for samples 2 and 3 were fitted according to eq 28 and 29 with numerical values listed in Table I. We have arbitrarily separated the results into two parts: one before the gel effect (eq 28) and the other in the presence of the gel effect. The longer induction period for sample 2 due to the presence of a much larger amount of the inhibitor is not shown.

It should be noted that the reaction rate is affected by the amount of inhibitor in MMA. This is one of the reasons why the proposed scheme will be useful for monitoring polymerization processes.

We have arbitrarily separated the polymerization process into two parts. The linear behavior with a constant reaction rate is represented by eq 28. A rapid increase occurs at about 5% of f_p for the thermal polymerization of MMA at 50 °C. The acceleration due to the "gel effect" has often been referred to as the Trommsdorf effect, which is accompanied by high viscosities. The relationship between the onset of the autoacceleration rate and solution properties of the monomer–polymer system has been discussed by many authors.[15-18] We shall use only a simple kinetic scheme[19] to represent the polymerization of MMA as shown in Figure 4:

$$\ln [(f_p - a_2)/(a_3 - f_p)] = a_4 + a_5 t \tag{29}$$

where the a_i's are the appropriate constants. The results are summarized in Table I.

2. Intensity of Scattered Light. By means of eq 27–29, we can determine the polymer concentration C_p at any time during the polymerization process. We shall now combine this information with light scattering (intensity) measurements to examine the molecular properties of the polymer product(s) formed. The intensity of scattered light at four different scattering angles (35, 60, 90, and 135°) were measured. By extrapolation to zero scattering

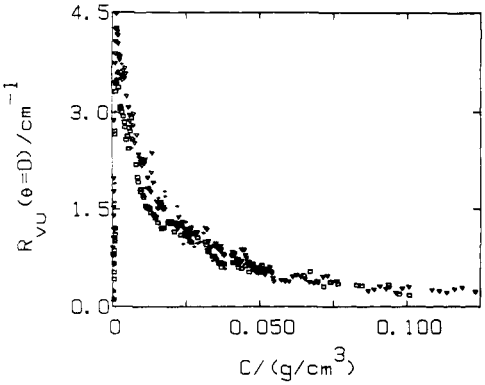

Figure 5. Rayleigh ratio $R_{vu}(\theta = 0)$ vs. concentration (g/cm^3) for sample 1 (plus signs), sample 2 (hollow squares), and sample 3 (inverted hollow triangles).

Table II
Molecular Parameters in Dilute Solution

sample	$M_w \times 10^{-6}$	A_2, mol cm^3 g^{-2}	R_g, nm	C^*, g/cm^3
1	2.00	2.0×10^{-4}	52.2	2.33×10^{-2}
2	3.70	1.8×10^{-4}	74.5	1.49×10^{-2}
3	4.54	1.5×10^{-4}	84.5	1.24×10^{-2}

angle and subtracting the scattered intensity of MMA, we have determined $R_{vu}(\theta = 0)$ as a function of concentration for samples 1, 2, and 3, as shown in Figure 5. Sample 1 (90 °C) exhibits intensity behaviors slightly different from those of samples 2 and 3 (both at 50 °C). For example, the maximum for sample 1 occurs at a slightly higher concentration than those of samples 2 and 3. We shall return to this data set after we have made an analysis first in dilute solutions.

In a free radical polymerization process we know that the polymer molecular weight remains relatively constant during the initial polymerization process. So in a Zimm plot as illustrated in Figure 6 for samples 1, 2, and 3, we can determine the molecular weight M_w, the second virial coefficient A_2, and the radius of gyration R_g of the polymer product(s) formed according to eq 1–4. The polymer concentration C_p was determined by means of eq 27–29 by using conversion data of Figure 4 from Raman scattering. The results are summarized in Table II. The linear behavior in the Zimm plots strongly suggests our supposition that the molecular weight of the polymer indeed remains constant. The top, middle, and bottom parts of Figure 6 represent the thermal polymerization of MMA to form PMMA under three different conditions. Meaningful results can be achieved at different polymerization temperatures with different amounts of inhibitors. It further implies why the maximum for sample 1 in Figure 5 occurs at a slightly higher concentration. Conversely, from $R_{vu}(\theta = 0)$, we can always determine M_w in dilute solutions if A_2 and C are known. In semidilute solutions, we may want to examine the static property of the polymer solution in terms of $M(\partial\pi/\partial C)/RT$ as a function of reduced concentration C/C^*, where C^* ($\equiv M/N_A R_g^3$) is the overlap concentration as shown in Figure 7 and Table II.

The universal curve in the molecular weight range which we have illustrated can be represented by straight lines over limited ranges in the semidilute solution regime, as shown in Figure 7. Measurements of the osmotic compressibility in semidilute solutions permit us to determine the polymer concentration independent of the polymer molecular weight. The solid straight line in Figure 7 can be represented by

$$M(\partial\pi/\partial C)/RT = k_M(C/C^*)^m \qquad (30)$$

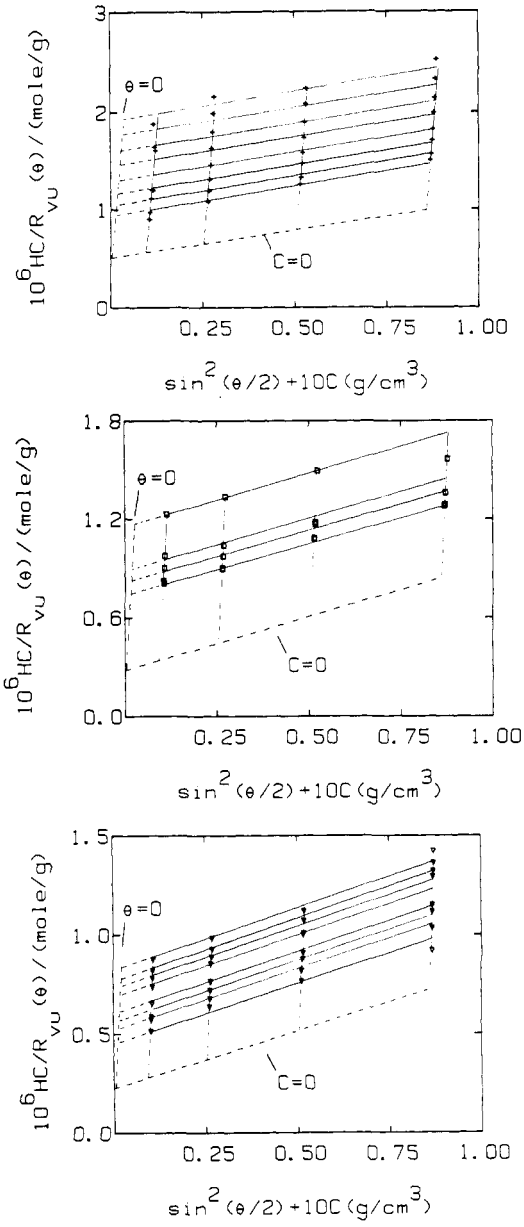

Figure 6. (Top) Zimm plot for sample 1. Distilled MMA + 1 drop of undistilled MMA (representing introduction of a trace amount of inhibitor) thermally polymerized at 90 °C. (Middle) Zimm plot for sample 2. Undistilled MMA (with inhibitor) thermally polymerized at 50 °C. (Bottom) Zimm plot for sample 3. Distilled MMA + 1 drop of undistilled MMA (representing introduction of a trace amount of inhibitor) thermally polymerized at 50 °C.

where m varies from an initial slope of 1.3 at low ranges of C/C^* (<1) to ~2 for $C/C^* > 2$. According to the scaling law, $m = 1/(3\alpha_R - 1)$, i.e., 1.3 and 2 for $\alpha_R = 0.59$ and 0.50, respectively. The crossover region is very broad from dilute to semidilute concentrations. We note that in the limit of zero concentration, eq 4 and 5 combine to yield

$$\lim_{C\to 0} (\partial\pi/\partial C)/RT = 1/M_w \qquad (31)$$

Therefore, the universal curve in Figure 7 starts at values very slightly higher than 1 in dilute concentrations and it increases with increasing concentration because of a positive A_2 in good solvent, such as our system of PMMA in MMA. However, A_2 is related to M and C^*. So, the universal curve is valid over the entire concentration range from dilute to semidilute solutions, including the crossover region. More quantitative behavior using renormalization group techniques has been reported.[20] Therefore, in fairly

Table III
Numerical Parameters in Time Correlation Function Profile Analysis Using Single-Exponential Fit, Second-Order Cumulant Method, and When Applicable, the Multiexponential Singular-Value Decomposition Technique

	Figure 9			
	top plot	second plot	third plot	bottom plot
1. Sample Identification ($\theta = 35°$)				
sample	2	3	3	3
reaction time, h	3	4	31.5	124
concentration, g/cm^3	1.34×10^{-3}	8.59×10^{-4}	6.71×10^{-3}	2.60×10^{-2}
2. Single-Exponential Fit				
Γ, s^{-1}	1.81×10^{3}	1.35×10^{3}	815	1.55×10^{4}
D, cm^2/s	1.54×10^{-7}	1.15×10^{-7}	6.94×10^{-10}	1.32×10^{-6}
3. Second-Order Cumulant Fit				
$\bar{\Gamma}$, s^{-1}	2.22×10^{3}	1.72×10^{3}	15.9	1.64×10^{4}
$\bar{D}$, cm^2/s	1.89×10^{-7}	1.46×10^{-7}	1.35×10^{-9}	1.39×10^{-6}
$\mu_2/\bar{\Gamma}^2$	0.20	0.21	1.06	0.06
4. Third-Order Cumulant Fit				
$\bar{\Gamma}$, s^{-1}			28.3	
$\bar{D}$, cm^2/s			2.31×10^{-9}	
$\mu_2/\bar{\Gamma}^2$			1.66	
5. Multiexponential Fit				
$\bar{\Gamma}$, s^{-1}	2.29×10^{3}	1.78×10^{3}		
$\bar{D}$, cm^2/s	1.95×10^{-7}	1.51×10^{-7}		
$\mu_2/\bar{\Gamma}^2$	0.26	0.27		

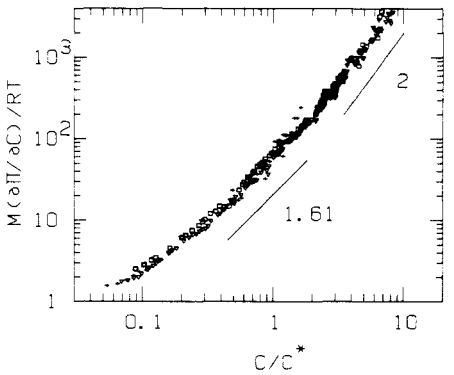

Figure 7. log–log plot of $M(\partial\pi/\partial C)/RT$ vs. C/C^* for sample 1 (plus signs), sample 2 (hollow squares), and sample 3 (inverted hollow triangles).

good solvents, Figure 7 can be used to extract the polymer concentration from measurements of absolute scattered intensity at zero scattering angle ($R_{vu}(\theta \to 0)$) provided that the refractive index increment of the polymer–solvent system is known. While theory deals mainly with monodisperse polymers, an experiment on the thermal polymerization of MMA yields PMMA with a fairly polydisperse distribution, i.e., $M_w/M_n \sim 2$. In constructing this particular universal curve, we have implicitly assumed that the polydispersity effect is negligible since π is independent of molecular weight in semidilute solutions. The fact that the data points do overlap suggests that it is valid for us to make such approximations. Furthermore, the agreement between the theoretical and the experimental value for m at $C/C^* \sim 1$ strengthens our suppositions, which will again be verified by our light scattering line width measurements. It should be noted that once we have demonstrated such a universal curve from experiments, its utility is not restricted to PMMA in MMA. Changes of polydispersity will invariably affect the crossover region in the universal curve; but the application can certainly be expanded to polymer products with fairly constant broad molecular weight distributions.[20] In Figure 7, the universal curve is likely to break down if we try to approach the Θ condition or to go below the Θ temperature for high molecular weight polymers, where we may encounter critical effects in the crossover region,[21] because in this simple scaling plot we have not fully taken into account all of the effects due to solvent quality. We may also construct a log–log plot of $(\partial\pi/\partial C)/RT$ vs. C as a function of M as shown in Figure 8, where we have demonstrated how M can be determined from such a surface in dilute solutions if $(\partial\pi/\partial C)/RT$ and C are known.[3] At constant temperature, Figure 8 can be collapsed to one universal curve as shown in Figure 7 over the entire concentration range from dilute to semidilute solutions. The experimental surface as shown in Figure 8 becomes parallel to the molecular weight axis in semidilute solutions, indicating $(\partial\pi/\partial C)_{P,T}$ to be essentially independent of molecular weight.

3. Spectrum of Scattered Light. Figure 9 shows typical plots of $G_k^{(2)}(\tau)$ and % dev as a function of delay channel number during the polymerization process, where

$$\%\ \text{dev} = \frac{(Ab)^{1/2}|g^{(1)}(\tau)|_{\text{measd}} - (Ab)^{1/2}|g^{(1)}(\tau)|_{\text{calcd}}}{(Ab)^{1/2}|g^{(1)}(\tau)|_{\text{measd}}} \times 100 \tag{32}$$

where $(Ab)^{1/2}_{\text{measd}}$ and $(Ab)^{1/2}_{\text{calcd}}$ may not be the same.

In the initial analysis, we used the second-order cumulant method[22] with

$$Ab|g^{(1)}(\tau)|^2 = Ab \exp\{2[-\bar{\Gamma}\tau + (1/2)(\mu_2/\bar{\Gamma}^2)(\bar{\Gamma}\tau)^2]\} \tag{33}$$

where $\mu_2 = \int G(\Gamma)(\Gamma - \bar{\Gamma})^2\, d\Gamma$ and $\bar{\Gamma} = \int G(\Gamma)\Gamma\, d\Gamma$. Some of the results of our analysis in Figure 9 are listed in Table III. The first and second plots of Figure 9 show the time correlation functions in the beginning of the polymerization process when the polymer solution concentration is relatively low. In dilute solutions, we have made single-exponential, cumulant, and multiexponential analyses. The $\bar{D}_T$ and $\mu_2/\bar{\Gamma}^2$ values are and should be in reasonable agreement using the method of cumulants and the multiexponential model because both approaches try to take into account the polydispersity effect. However, in view of the broader size distributions, there are more uncertainties associated with the second-order cumulant method because we cannot use only the $\bar{\Gamma}$ and μ_2 terms to force fit

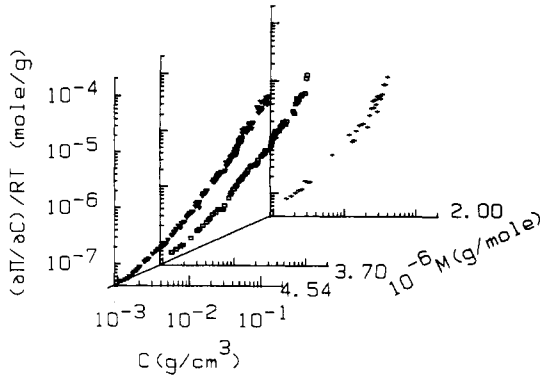

Figure 8. Three-dimensional plot of osmotic compressibility $(\partial\pi/\partial C)_{P,T}$ as a function of concentration and molecular weight for PMMA in MMA, see also Figure 1 of ref 3 for polystyrene in *trans*-decalin at 45 °C. It should be recognized that the osmotic compressibility becomes independent of polymer molecular weight in semidilute solutions. Therefore, the log $(\partial\pi/\partial C)_{P,T}$ vs. log C vs. M surface is parallel to M in semidilute solutions.

the time correlation function $|g^{(1)}(\tau)|$ of a fairly polydisperse polymer solution. For polydisperse polymer solutions the single-exponential model does not represent the measured time correlation function and it can only be used as an estimate to other more complex models.

The application of eq 33 is delicate as it is difficult to determine whether we have fitted the measured time correlation function in the appropriate frequency range. Values of $\bar{\Gamma}$ can remain reliable even for fairly broad line width distributions ($\mu_2/\bar{\Gamma}^2 \lesssim 0.3$); but values of μ_2 can be in error easily by as much as 50%. The multiexponential fit yields reliable values for both $\bar{\Gamma}$ and μ_2.

In semidilute solutions, the faster cooperative diffusion coefficient D_c is independent of molecular weight and can be fitted with a single-exponential function while the slow mode which is now assumed to be proportional to D_s depends upon molecular weight as shown by eq 9. Furthermore, as R_g = 84.5 nm and KR_g = 2.15 at θ = 90° for sample 3, we cannot use $\bar{\Gamma}_s = \bar{D}_s K^2$. Instead, we assume that the structure factor correction[23] for internal motions of polymer coils in dilute solution

$$\bar{\Gamma} = K^2\bar{D}_T(1 + fR_g^2K^2 + ...) \quad (34)$$

is applicable to $\bar{D}_s$ in semidilute solutions and write

$$\bar{\Gamma}_s = K^2\bar{D}_s(1 + fR_g^2K^2 + ...) \quad (35)$$

where $f = {}^1/_5$ and ${}^1/_6$ without and with preaveraging of the hydrodynamic interactions for linear polydisperse polymer coils with a Flory "most probable" distribution. From eq 35, we get $\bar{D}_{slow} = 2.22 \times 10^{-9}$ and 2.23×10^{-9} cm²/s at θ = 35° and 90°, respectively, and $C = 6.72 \times 10^{-3}$ g/cm³ using $f = {}^1/_6$ and R_g = 84.5 nm at both scattering angles. For sample 3, $C^* = 1.25 \times 10^{-2}$ g/cm³, which is greater than $C = 6.72 \times 10^{-3}$ g/cm³. However, for polymer viscoelastic fluids, we have the crossover concentration C_e, representing the onset of entanglement behavior. In Θ solutions, $C_e < C^*$. Figure 10 shows log–log plots of $\bar{D}_{slow}$ and $\bar{D}_c$ as a function of concentration in semidilute solutions. The experimental curves exhibit slopes which are in very good agreement with theoretical predictions as listed in Table IV. From here on, we identify D_{slow} behavior with D_s behavior and let $D_{slow} \equiv D_s$.

In computing D_s from correlation function measurements obtained at θ = 90°, we have found $f \approx {}^1/_6$ to be a reasonable correction factor for eq 35, as shown in Figure 10, where $\bar{D}_s$ values measured at different concentrations and at θ = 35° and 90° are in reasonable agreement. The second-order cumulant method is *approximately* valid in

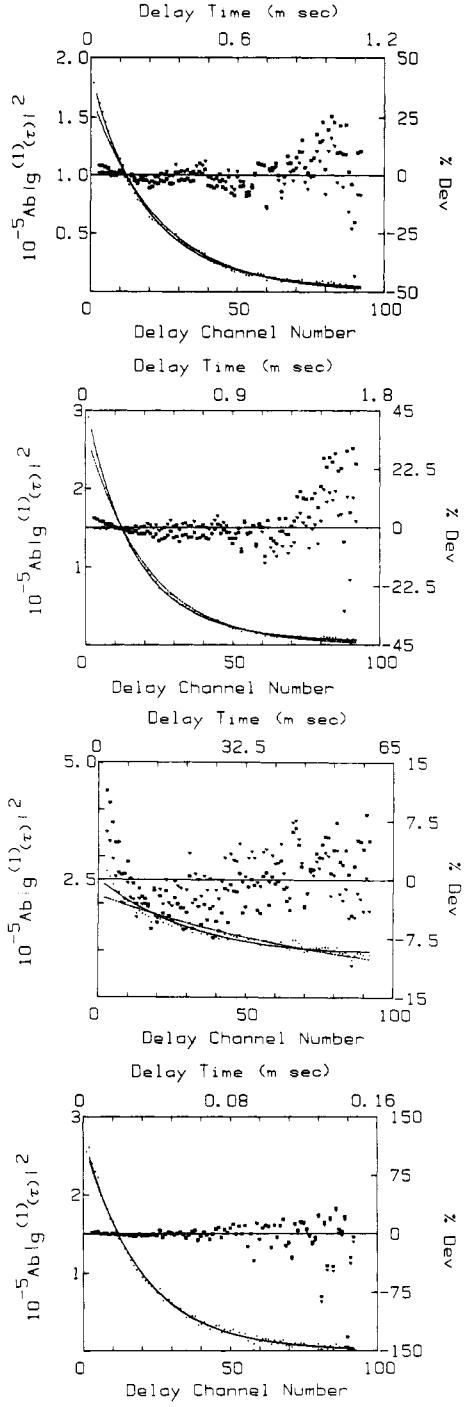

Figure 9. Typical plots of $Ab|g^{(1)}(\tau)|^2$ and % dev vs. delay channel number and delay time for samples 2 and 3. Numerical parameters are listed in Table III. Top plot: delay time increment = $\Delta\tau$ = 12 μs. Solid curve is represented by $Ab|g^{(1)}(\tau)|^2 = 1.87 \times 10^5 \exp\{2[-2.22 \times 10^3\tau + {}^1/_2(9.84 \times 10^5)\tau^2]\}$. The dash–double dot curve is represented by $Ab|g^{(1)}(\tau)|^2 = 1.69 \times 10^5 \exp(-3.62 \times 10^3\tau)$. Second plot: $\Delta\tau$ = 18 μs. Solid curve is represented by $Ab|g^{(1)}(\tau)|^2 = 3.10 \times 10^5 \exp\{2[-1.72 \times 10^3\tau + {}^1/_2(6.12 \times 10^5)\tau^2]\}$. The dash–double dot curve is represented by $Ab|g^{(1)}(\tau)|^2 = 2.73 \times 10^5 \exp(-2.70 \times 10^3\tau)$. Third plot: $\Delta\tau$ = 650 μs. Solid curve is represented by $Ab|g^{(1)}(\tau)|^2 = 2.83 \times 10^5 \exp\{2[-28.3\tau + {}^1/_2(1.33 \times 10^2)\tau^2 - {}^1/_6(1.80 \times 10^4)\tau^3]\}$. The dash–double dot curve is represented by $Ab|g^{(1)}(\tau)|^2 = 2.51 \times 10^5 \exp\{2[-(15.9\tau + {}^1/_2(2.70 \times 10^2)\tau^2]\}$. Bottom plot: $\Delta\tau$ = 1.6 μs. Solid curve is represented by $Ab|g^{(1)}(\tau)|^2 = 2.76 \times 10^5 \exp\{2[-1.64 \times 10^4\tau + {}^1/_2(1.59 \times 10^7)\tau^2]\}$. The dash–double dot curve is represented by $Ab|g^{(1)}(\tau)|^2 = 2.69 \times 10^5 \exp(-3.11 \times 10^4\tau)$. In the deviation plots, the top, second, and bottom plots have hollow squares representing single-exponential fits and third plot has hollow squares representing a third-order cumulant fit. All inverted hollow triangles represent a second-order cumulant fit.

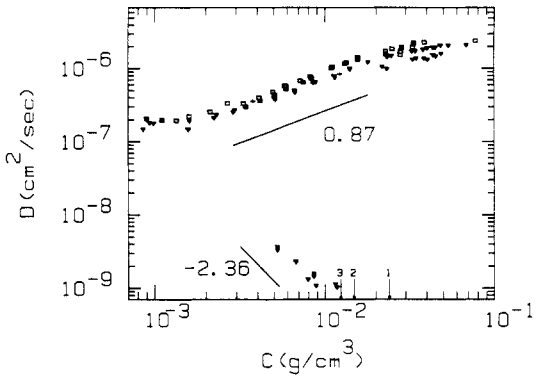

Figure 10. log–log plots of diffusion coefficients $\bar{D}_s$ and D_c vs. concentration of sample 1 measured at $\theta = 35°$ (plus signs), sample 2 at $\theta = 35°$ (hollow squares) and $\theta = 90°$ (filled squares), and sample 3 at $\theta = 35°$ (inverted hollow triangles) and $\theta = 90°$ (inverted filled triangles). 1, 2, and 3 on the abscissa represent C^* values for samples 1, 2, and 3. $\bar{D}_s$ corresponds to the slow mode.

Table IV
Numerical Values of Limiting Slopes[a] according to Scaling Laws for Osmotic Compressibility, Cooperative Diffusion Coefficient, and Self-Diffusion Coefficient

$M(\partial\pi/\partial C)/RT = k_M(C/C^*)^m$ with $m = 1/(3\alpha_R - 1)$

α_R	m	obsd slope in Figure 7 for $C/C^* < 1$
0.5	2	
0.54	1.61	1.61
0.6	1.25	

$\bar{D}_s = k_s M^{-2} C^{(\alpha_D - 2)/(3\alpha_D - 1)}$

α_D	$(\alpha_D - 2)/(3\alpha_D - 1)$	obsd slope in Figure 10
0.5	-3	
0.54	-2.36	-2.36
0.6	-1.75	

$D_c = k_c C^{\alpha_D/(3\alpha_D - 1)}$

α_D	$\alpha_D/(3\alpha_D - 1)$	obsd slope in Figure 10
0.5	1	
0.54	0.87	0.87
0.6	0.75	

[a] It should be noted that $0.6 > \alpha_R > 0.54$ and $\alpha_R > \alpha_D$ for our PMMA in MMA.

the evaluation of $\bar{D}_s$ because we have observed a fairly large variance for $\bar{D}_s$. However, since the time correlation functions for $\bar{D}_s$ contain more noise, we have attempted to use the cumulant method only up to third-order, in order to determine more precise values of $\bar{D}_s$ and $\mu_s/\bar{\Gamma}_s^2$. Nevertheless, it is satisfying to note that the slopes expressing the concentration dependence of $(\partial\pi/\partial C)_{T,P}/RT$ in Figure 7 and those of D_c and $\bar{D}_s$ (third-order cumulant fit) in Figure 10 are self-consistent over the limited concentration range $C/C^* \leq 1$ as listed in Table IV. We may conclude from our analysis that the entanglement concentration in shear viscosity, C_e, describes a better dynamical crossover regime from Rouse-like motions to reptation because $\bar{D}_s$ and D_c can be measured below C^*, that the power law is valid only over a very limited concentration range in semidilute solutions, because the curves are not really straight lines, and that according to Figure 7, a log–log plot of $M(\partial\pi/\partial C)/RT$ vs. C/C^* exhibits universal behavior over the entire concentration range, including crossover regions from dilute to semiconcentrated solutions. As the cooperative diffusion coefficient is independent of molecular weight, the top plot of Figure 9 clearly demonstrates that the time correlation function for

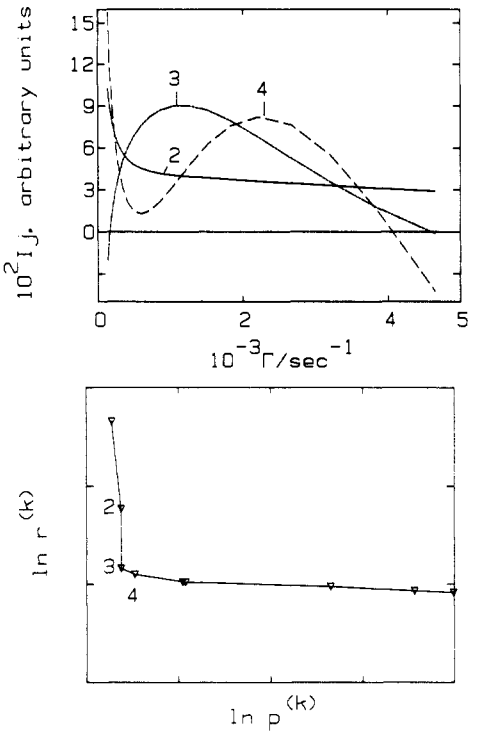

Figure 11. (Top) Plots of line width distributions in I_j vs. Γ based on candidate solutions in $p^{(k)}$ with $k = 2$, 3, and 4 for sample 3 at $\theta = 35°$ and $C = 8.59 \times 10^{-4}$ g/cm³. The norm of the solution vector $||p^{(k)}||$ is defined by $||p^{(k)}|| = [\sum_{j=1}^{N} I_j^2]^{1/2}$, with N being the number of δ functions used in the approximation for $G(\Gamma)$. (Bottom) Plot of logarithm of residual norm $||r^{(k)}||$ vs. logarithm of $||p^{(k)}||$. $||r^{(k)}|| = [\sum_{j=1}^{M}(|g^{(1)}(\tau)_{expt}| - |g^{(1)}(\tau)_{calcd}|)^2]^{1/2}$, with M being the number of data points in the correlation function. The $k = 3$ solution is postulated on the optimal solution as it has the lowest solution vector norm with an acceptably low residual norm.

D_c has a single-exponential behavior with $\Gamma = 1.55 \times 10^4$ s^{-1} using a single-exponential fit and $\bar{\Gamma} = 1.63 \times 10^4$ s^{-1} using a second-order cumulant fit where $\mu_2/\bar{\Gamma}^2 = 0.06$, confirming essentially the single-exponential behavior. The internal consistency exhibited by the slopes in Figures 7 and 10 also suggests that the molecular weight of the polymer product formed remains relatively constant in semidilute solutions ($C/C^* \gtrsim 1$) because $\bar{D}_s$ depends on the polymer molecular weight and could not exhibit a slope obeying the values listed in Table IV if the polymer molecular weight (or clustering behavior) changes during the polymerization process. The curvatures shown respectively in Figures 7 and 10 for $(\partial\pi/\partial C)_{P,T}$ and D_c are independent of polymer molecular weight.

4. Molecular Weight Distribution Analysis. In dilute solution, we can relate the line width distribution function to the molecular weight distribution function.[12,24] So, it is worthwhile to make an approximate Laplace transform of $g^{(1)}(\tau)$ using the multiexponential model. By means of the singular-value decomposition technique, we can obtain an approximate $G(\Gamma)$ as shown in the top part of Figure 11. The $k = 3$ solution yields the best fit according to our minimization scheme,[11] as shown in the bottom portion of Figure 11.

Figure 12 shows $Ab|g^{(1)}(\tau)|^2$ and % dev as a function of delay channel number for the same sample 3 at $C = 8.59 \times 10^{-4}$ g/cm³ and $\theta = 35°$, where the candidate solutions in terms of $G(\Gamma)$ for $k = 2$, 3, and 4 have been expressed in Figure 11. It should be recognized that the $k = 3$ candidate solution is selected not only because it shows the minimum in the bottom portion of Figure 11 but also because we know physically that I_j is positive and $G(\Gamma)$ is essentially unimodal. Figure 13 shows that the shape

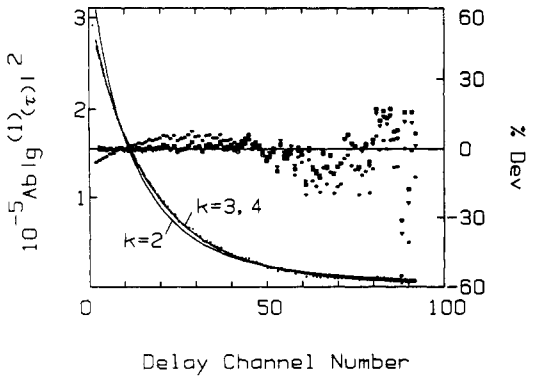

Figure 12. Plot of $Ab|g^{(1)}(\tau)|^2$ and % dev vs. delay channel number for the same sample and conditions as in Figure 11. Numerical values from the multiexponential fit $G(\Gamma)$ have been presented in Figure 11. In the % dev plot, k = 2 (*), 3 (□), and 4 (▼).

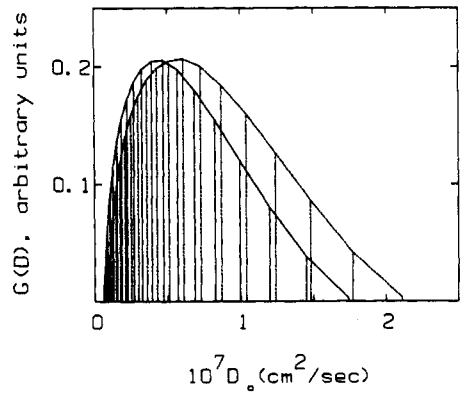

Figure 13. Unnormalized line width distribution for sample 2 (dash–double dot curve) at k = 3, $C = 1.34 \times 10^{-3}$ g/cm^3, and θ = 35° (same data as in Figure 9, top) and sample 3 (solid curve) at k = 3, $C = 8.59 \times 10^{-4}$ g/cm^3, and θ = 35° (same data as in Figure 9, second plot). Note that we have used eq 8 to shift the x axis to D_0 [$=D/(1 + k_DC)$], with $k_D = 0.943 \times 10^3$ cm^3/g.

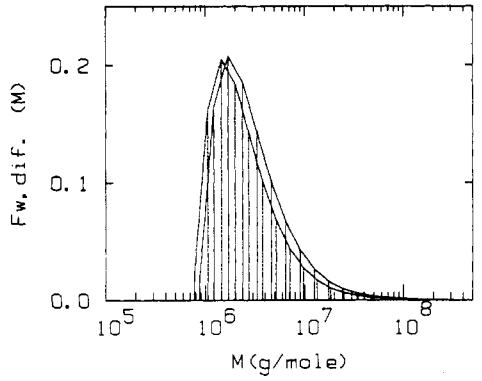

Figure 14. Molecular weight distributions for samples 2 (dash–double dot curve) and 3 (solid curve) with α_D = 0.56.

of $G(\Gamma)$ for sample 2 and the shape of $G(\Gamma)$ for sample 3 are similar, with $\bar{D} = 1.95 \times 10^{-7}$ cm^2/s for sample 2 and 1.51×10^{-7} cm^2/s for sample 3. On the basis of discussions related to eq 13–19, we can transform a plot of $G(D_0)$ vs. D_0 into a plot of $F_{w,dif}$ vs. M, where $F_{w,dif}$ is the polymer differential molecular wieght function with an "assumed" α_D = 0.56, as has been justified indirectly in Table IV. Figure 14 shows the molecular weight distributions of PMMA obtained by thermal polymerization of MMA with different amounts of inhibitors (samples 2 (dash–double dot curve) and 3 (solid curve) with α_D = 0.56). The consistency of our results can best be expressed in Table V, which shows effects of α_D values on the polydispersity index M_w/M_n. For $\alpha_D \sim 0.55$, $M_w/M_n \sim 2$ for samples

Table V
Effects of α_D on the Polydispersity Index M_w/M_n

α_D	M_w/M_n sample 2	M_w/M_n sample 3
0.50	2.08	2.19
0.52	2.01	2.14
0.54	1.97	2.07
0.56	1.91	2.01
0.58	1.87	1.96
0.60	1.82	1.91

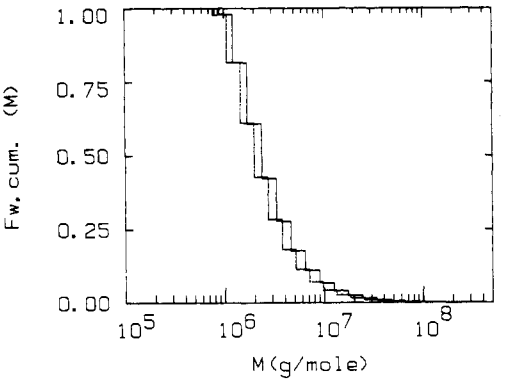

Figure 15. Cumulative molecular weight distributions for samples 2 (dash–double dot histogram) and 3 (solid histogram) based on the analysis of Figure 14.

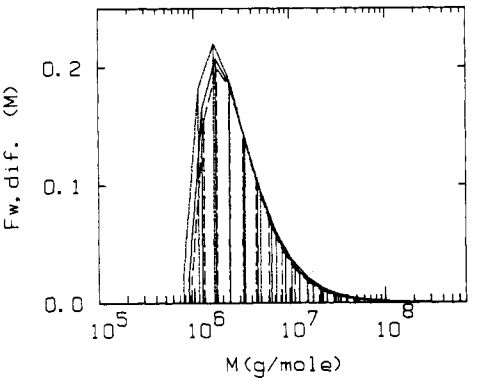

Figure 16. Molecular weight distributions for sample 3 with α_D = 0.5 (dash–double dot curve), α_D = 0.56 (solid curve), and α_D = 0.6 (dashed curve).

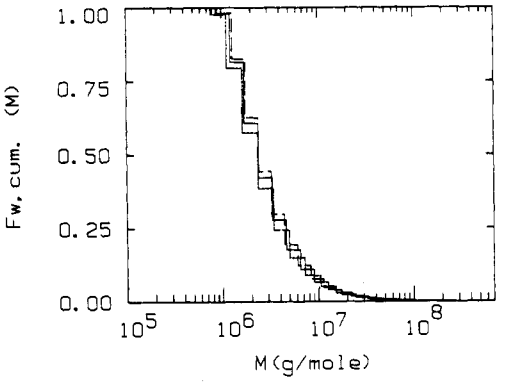

Figure 17. Cumulative molecular weight distributions for sample 3 with α_D = 0.5 (dash–double dot histogram), α_D = 0.56 (solid histogram), and α_D = 0.6 (dashed histogram).

2 and 3, in good agreement with the theoretical prediction of 2 for the thermal polymerization of MMA in the dilute solution region. Figure 15 shows the cumulative molecular weight distribution $F_{w,cum}(M)$ based on the results of Figure 14. The molecular weight of PMMA varies over a range of about 30. It should be recognized that the value of M_w/M_n increases with decreasing α_D values as listed in

Table V and shown schematically in Figures 16 and 17. With small variations in α_D, such as 0.54–0.56, the results of our studies remain unchanged.

V. Conclusions

We have investigated many of the macromolecular parameters of PMMA in MMA during the thermal polymerization of MMA using a combination of Raman spectroscopy and laser light scattering. In the process, we have made use of the scaling concept to interpret the experimental data as well as the experimental data to support some aspects of the scaling theory. Our results are internally consistent in terms of the concentration behavior of osmotic compressibility, cooperative diffusion coefficient, and the very slow characteristic relaxation time (D_s). In dilute solutions, we have been able to determine the molecular weight distributions of PMMA as well as M_w, A_2, R_g, and k_D, provided that the PMMA molecular weight has remained relatively constant during the polymerization process. The linear concentration dependence in osmotic compressibility $(\partial\pi/\partial C)_{T,P}$ and the translational diffusion coefficient D_T seems to strengthen this supposition. Furthermore, in semidilute solutions, the concentration dependence of $\bar{D}_s$ follows the constant molecular weight behavior as shown in Figure 10 and Table IV. Thus, we have demonstrated a scheme whereby we can indeed investigate pertinent macromolecular parameters during solution polymerization kinetics.

In semidilute solutions, we have experimentally observed the slow mode at concentrations below $M_w/(N_A R_g^3)$, suggesting that the overlap concentration C_e is the more appropriate parameter. As the osmotic pressure becomes independent of molecular weight in semidilute solutions, we cannot use the osmotic compressibility to determine the polymer molecular weight. On the other hand, the universal curve in a plot of $(\partial\pi/\partial C)_{P,T}$ vs. C in semidilute solutions suggests that we can determine the polymer concentration in semidilute solutions by measuring only the osmotic compressibility. The universal curve in a plot of $M(\partial\pi/\partial C)_{P,T}/RT$ vs. C/C^* shows a broad range of crossover concentrations, signifying the relative inaccessibility of the asymptotic behavior for the scaling law exponents even with polymer molecular weights exceeding 10^6. As the cooperative diffusion coefficient is also independent of polymer molecular weight, the slow characteristic time (D_s) becomes the only accessible parameter capable of revealing information on polymer molecular weight in semidilute solutions. However, we should note that $\bar{D}_s$ ($\sim(M_n M_w)^{-1}$ differs from $\bar{D}_T$ ($\sim M_w^{-\alpha_D}$) in its averaging process even if eq 9 is valid. Therefore, $\bar{D}_s$ and $\bar{D}_T$ behave differently in a polydisperse system. Similarly, the variance of $\bar{D}_s$, $\mu_2/\bar{\Gamma}_s^2$, provides a curious relationship to the molecular weight averages, as shown in eq 25. In any case, analysis of $\bar{D}_s$ in a polydisperse system involves the use of the cumulant method or a multiexponential singular-value decomposition technique in order to account for the non-single-exponential behavior of $|g^{(1)}(\tau)|$. Furthermore, at $KR_g > 1$, we have to take into account the structure factor as expressed in eq 35. It is interesting to note that the expression computed by Stockmayer and Schmidt can be extended to $\bar{D}_s$ in semidilute solutions.

In the third plot of Figure 9 and Table III, we have noted that the mean characteristic time for the slow mode is very different whether we use a single-exponential fit or a second-order cumulant fit. In other words, the time correlation function requires a higher order cumulant fit. For second- and third-order cumulant fits, we get $\mu_2/\bar{\Gamma}_s^2 = 1.06$ and 1.66, respectively, while $\mu_2/\bar{\Gamma}_s^2 = 3.24$ according to eq 25. The effects of polydispersity on the self-diffusion coefficient have also been reported recently by Bernard and Noolandi.[25]

In our analysis, we have noted that we can monitor the evolution of polymer formation and, in dilute solutions, measure many important molecular parameters of the polymer product such as the weight-average molecular weight M_w, the z-average radius of gyration $\langle R_g^2\rangle_z^{1/2}$, second virial coefficients A_2 and k_D, the characteristic times associated with translation and its corresponding equivalent hydrodynamic radius R_h, and estimates of the size (or molecular weight) distribution. In semidilute solutions, the accessible quantities such as the osmotic compressibility $(\partial\pi/\partial C)_{P,T}$ and the cooperative diffusion coefficient D_c become independent of molecular weight. However, these quantities, while no longer properties of polymer molecular weight, can be used to compute polymer concentration if a correspondence relationship is known.

We have observed a very slow characteristic time which has been identified as the self-diffusion coefficient.[7-9] In addition to quasi-elastic light scattering (QLS), many different techniques, including radioactive tracers,[26] infrared densitometry,[27] NMR,[28] forced Rayleigh scattering (FRS),[29] and fluorescence photobleaching recovery,[30] have been used to measure the self-diffusion coefficient. Generally, $D_s \propto M^{-2}$ as determined by Klein,[27] Klein and Briscos,[31] Bartels et al.,[32] Yu and co-workers,[33] Kimmich and Bachus,[34] and Fleischer.[35] The M^{-2} result is in good agreement with the scaling theory (eq 9). However, there are exceptions.[28] The concentration dependence of $D_s \propto C^{-1.75}$ has been determined by Leger et al.[29] and by Amis and Han[7] and that of $D_s \propto C^{-3}$ by Han and co-workers.[36] Unfortunately, the absolute value of $\bar{D}_{slow}$ from quasi-elastic light scattering[7] is an order of magnitude lower than that from forced Rayleigh scattering[29] and NMR.[37,38] In any case, assignment of very slow characteristic times as observed by QLS to self-diffusive motions is open for discussion even though eq 9 with appropriate variations in the concentration exponent, as shown in Table IV and Figure 10 for PMMA in MMA, is almost certainly applicable as an empirical equation which permits us to estimate some molecular properties of the polymer (or its clusters) in semidilute solutions. It should be noted that in the present context we are mainly interested in using existing known scattering techniques to monitor polymerization processes. Therefore, the interesting question on the exact nature of the slow mode in semidilute solutions can be settled as a separate issue. Nevertheless, we can point to the fact that from measurements of the concentration and molecular weight dependence of the slow mode we can obtain additional information on the polymer product.

The interpretation and measurements on the cooperative diffusion coefficient may be more complex[38] because of the transient network lifetime τ_R. In Figure 10, we have noted a leveling of the concentration dependence of D_c at higher concentrations ($C > C^*$). This effect can best be explained in terms of two distinct elastic moduli in polymer solutions at semidilute concentrations:

$$D_c = [K_{os} + (4/3)G]/f \tag{36}$$

where K_{os}, G, and f are, respectively, the osmotic modulus, the shear modulus, and the frictional coefficient with concentration dependences of $K_{os} \sim C^3$, $G \sim C^2$, and $f \sim C^2$ in the Θ region. Thus, if G starts to dominate, the concentration dependence of D_c will level off. The details of this investigation represent a very interesting problem because we need to know the relations among K_{os}, G, f, τ_R, and K. We plan to utilize the polymerization reaction to produce well-characterized polymer solutions in semidilute

and semiconcentrated regimes to study the behavior of D_c. This represents the second aspect of our studies, i.e., to use the polymerization data to investigate some aspects of the scaling theory. Further experiments are in progress.

Acknowledgment. B.C. thanks Dr. G. Hagnauer of AMMRC, Watertown, MA, for his encouragement and gratefully acknowledges the U.S. Army Research Office for support of this research project.

Registry No. PMMA (homopolymer), 9011-14-7.

References and Notes

(1) Chu, B. "Lase Light Scattering"; Academic Press: New York, 1974. Berne, B. J.; Pecora, R. "Dynamic Light Scattering"; Wiley: New York, 1976.
(2) Chu, B.; Fytas, G.; Zalczer, G. *Macromolecules* **1981**, *14*, 395.
(3) Chu, B.; Fytas, G. *Macromolecules* **1982**, *15*, 561.
(4) Meeks, M.; Koenig, J. L. *J. Polym. Sci., Part A-2* **1971**, *9*, 717.
(5) Chu, B. In "Scattering Techniques Applied to Supramolecular and Nonequilibrium Systems"; Chen, S.-h., Chu, B., Nossal, R., Eds.; Plenum Press: New York, 1981; p 231.
(6) Chu, B. *J. Polym. Sci.*, to be published.
(7) Amis, E. J.; Han, C. C. *Polymer* **1983**, *23*, 1403.
(8) Amis, E. J.; Janmey, P. A.; Ferry, J. D.; Yu, H. *Polym. Bull.* **1981**, *6*, 13.
(9) Amis, E. J.; Janmey, P. A.; Ferry, J. D.; Yu, H. *Macromolecules* **1983**, *16*, 441.
(10) Chu, B. In "Correlation Function Profile Analysis in Laser Light Scattering. I. General Review on Method of Data Analysis", Proceedings of the NATO ASI on the Application of Laser Light Scattering to the Study of Biological Motions; Earnshaw, J. C., Steer, M. W., Eds.; Plenum Press: New York, 1983.
(11) Ford, J. R.; Chu, B. "Correlation Function Profile Analysis in Laser Light Scattering. III. An Iterative Procedure", Proceedings of the 5th International Conference on Photon Correlation Techniques in Fluid Mechanics; Schulz-DuBois, E. O., Ed.; Springer-Verlag: New York, 1983; pp 303–314.
(12) Chu, B.; Ford, J. R.; Pope, J. *Soc. Plast. Eng.* [*Tech. Pap.*] **1983**, *26*, 547.
(13) de Gennes, P.-G. "Scaling Concepts in Polymer Physics"; Cornell University Press: Ithaca, NY, 1979.
(14) Huglin, M. B., Ed. "Light Scattering from Polymer Solutions"; Academic Press: New York, 1972.
(15) O'Driscoll, K. F. *Pure Appl. Chem.* **1981**, *53*, 617.
(16) Balke, S. T.; Hamielec, A. E. *J. Appl. Polym. Sci.* **1973**, *17*, 905.
(17) Tulig, T. J.; Tirrell, M. *Macromolecules* **1981**, *14*, 1501.
(18) Tulig, T. J.; Tirrell, M. *Macromolecules* **1982**, *15*, 459.
(19) Sawads, H. *J. Polym. Sci., Part B* **1963**, *1*, 305.
(20) Oono, Y.; Ohta, T.; Freed, K. F. *J. Chem. Phys.* **1981**, *74*, 6488.
(21) Chu, B.; Nose, T. *Macromolecules* **1980**, *13*, 122.
(22) Koppel, D. E. *J. Chem. Phys.* **1972**, *57*, 4814.
(23) Stockmayer, W. H.; Schmidt, M. *Pure Appl. Chem.* **1982**, *54*, 407.
(24) DiNapoli, A.; Chu, B.; Cha, C. *Macromolecules* **1982**, *15*, 1174.
(25) Bernard, D. A.; Noolandi, J. *Macromolecules* **1983**, *16*, 548.
(26) Bueche, F. *J. Chem. Phys.* **1968**, *48*, 1410.
(27) Klein, J. *Nature (London)* **1978**, *271*, 143.
(28) Tanner, J. E. *Macromolecules* **1971**, *4*, 748.
(29) Leger, L.; Hervet, H.; Rondelez, F. *Macromolecules* **1981**, *14*, 1732.
(30) Smith, B. A. *Macromolecules* **1982**, *15*, 469.
(31) Klein, J.; Briscoe, B. J. *Proc. R. Soc. London, Ser. A* **1979**, *365*, 53.
(32) Bartels, C. R.; Graessley, W. W.; Crest, B. *J. Polym. Sci., Polym. Lett. Ed.* **1983**, *21*, 495.
(33) Yu, H., private communication.
(34) Kimmich, R.; Bachus, R. *Colloid Polym. Sci.* **1982**, *260*, 911.
(35) Fleischer, G. *Polym. Bull.* **1983**, *9*, 152.
(36) Han, C., private communication.
(37) Callaghan, P. T.; Pinder, D. N. *Macromolecules* **1980**, *13*, 1085; **1981**, *14*, 1334; **1983**, *16*, 968.
(38) Brochard, F. *J. Phys. (Paris)* **1983**, *44*, 39.

Polymerizable Built Up Multilayers on Polymer Supports

Otto Albrecht, André Laschewsky, and Helmut Ringsdorf*

Johannes Gutenberg-Universität, Institut für Organische Chemie, D-6500 Mainz, West Germany. *Received June 13, 1983*

ABSTRACT: Polymeric Langmuir–Blodgett (LB) multilayers[1] of the cadmium salt of hexacosa-10,12-diynoic acid were investigated on gas-permeable polypropylene supports. Although the multilayer films are macroscopically homogeneous, scanning electron microscopy revealed the influence of the support surface structure on the microscopic perfectness of the deposited layers. The polymerization conditions and the surface pressure during the monolayer deposition were varied and did not show any effect on the surface structure of the multilayers. Such polymeric LB composite membranes reduce the gas flow of CH_4 markedly. Thus, such membranes may be well suited for gas separation.

Introduction

Recent work on the application of monolayers and multilayer systems[2,3] has included the use for separation processes.[4–6] Analogous to the biological cell membrane, LB multilayers and liposomes—as comparable, support-free systems—should be well suited for separation purposes, because of their extreme thinness and their overall microscopically defined structure.

To overcome the lack of mechanical and chemical stability, reactive amphiphiles had been polymerized in multilayers[7,8] and in liposomes[9] several years ago. It was shown that LB multilayers and polymerized liposomes show retention of ions and large molecules in aqueous systems.[10,11] In this paper we discuss the potential application of LB multilayers for gas separation. In the initial state of our work, we used amphiphilic diacetylenes. It is well-known that diacetylenes only polymerize under topochemical control to yield deeply colored polymers.[12,13] The color gives an indication of the homogeneity of the supported multilayer, the presence of macroscopic defects in the layers, and the progress of the polyreaction. On the basis of investigations of various amphiphilic diacetylenes on various support materials,[14,15] we carried out detailed studies with the cadmium salt of hexacosa-10,12-diynoic acid (1) on three different polypropylene supports. The surface structure of the LB films and the gas retention of such LB composite membranes were investigated.

$$CH_3(CH_2)_{12}-C\equiv C-C\equiv C-(CH_2)_8COOH$$
1

Experimental Section

Materials. The synthesis of hexacosa-10,12-diynoic acid is described elsewhere.[16] The cadmium chloride was pure grade (Merck). The water was distilled and purified by a Millipore water purification system (Milli Q, Millipore Corp.). The polypropylene

0024-9297/84/2217-0937$01.50/0